Journal of Global Positioning Systems (2026)
Vol. 22, Issue 1:126-142
DOI:10.5081/jgps.22.1.126

Journal of Global Positioning Systems
2026
© CPGPS

A subsidence and spatial information monitoring system for mined-out regions: a case study in Jiawang, Xuzhou

Dongsheng Zhao [1,2], Hao Liu [2], Qianxin Wang (✉)[1,2], Kefei Zhang (✉)[1,2], Jianfeng Zha [1,2], Craig M. Hancock [3]

1 Observation and Research Station of Jiangsu Jiawang Resource Exhausted Mining Area Land Restoration and Ecological Succession, Ministry of Education, China University of Mining and Technology, Xuzhou 221116, China;

2 School of Environment and Spatial Informatics, China University of Mining and Technology, Xuzhou 221116, China;

3 School of Architecture Building and Civil Engineering, Loughborough University, Loughborough Leicestershire LE11 3TU, UK.

✉ the corresponding author, wqx@cumt.edu.cn; profkzhang@cumt.edu.cn

Abstract: Building subsidence, atmospheric water vapor, and ionospheric disturbances are essential key information for ecological restoration and high-quality development in mined-out areas. In this study, a subsidence and spatial information monitoring system was established in Jiawang, Jiangsu, which consists of a GNSS geodetic receiver, an ionospheric scina Experimental results show that the geographical environment in the area has been stable over the long term, with no significant relative position tilt observed in buildings. The GNSS-derived PWV time series, with a temporal resolution of 30 s, showed temporal variations corresponding to the evolution of the radar-observed precipitation event. The TEC and ionospheric disturbance indices captured the diurnal variations and disturbance characteristics during the selected space-weather event. The subsidence monitoring, atmospheric water vapor inversion, and ionospheric parameter monitoring conducted in Jiawang are crucial for the restoration of subsidence and the recovery of the mined-out area's productivity.

Keywords: GNSS, Ionosphere Scintillation, Subsidence Monitoring, Atmospheric Water Vapor

1. Introduction

After the completion of underground mining and a long period of natural compaction, the underground cavities and irregular rock mass cracks formed after mining will exist for a long time. Any disturbance may break the existing balance in the overlying rock, resulting in the secondary movement and deformation of the mined-out region and its overlying rock, thereby leading to the subsidence, partial cracking, tilting and other damages of the ground buildings, and even serious casualties and property losses [1][2]. Atmospheric water vapor is an important parameter not only for predicting regional climate change, rainfall and disastrous weather, but also for causing landslides and other geological disasters [3][4][5][6]. As an important part of the sun-terrestrial environment, drastic changes in electron content and ionospheric irregularities in the ionosphere can cause severe interference to short-wave and navigation satellite signal transmission, thereby affecting positioning, navigation and timing (PNT) services of the global navigation satellite system (GNSS), which is of highly importance in subsidence monitoring and position reference service for the mined-out region [7][8][9][10]. Therefore, an investigation of the subsidence monitoring, atmospheric water vapor and ionospheric parameters are particularly important for reparation of the subsidence and the restoration of production in the mined-out region.

Recently, the main technical means for monitoring subsidence in mined-out regions are GNSS and static leveling technology. When using GNSS to monitor surface subsidence, the absolute value of subsidence can be obtained, but the accuracy of the vertical direction is not high due to the influence of satellite constellation design. The static leveling system has advantages in automation and accuracy, and is currently widely used in the monitoring of building subsidence. The static leveling system is a precision measurement system that measures the relative vertical height changes between two or more points using the principle of connected vessels, namely the liquid in connected vessels has the same potential energy. It is a powerful complement to the absolute subsidence obtained by GNSS.

Due to the advantages of low monitoring cost, high temporal resolution, and fast response time, GNSS is highly suitable for atmospheric water vapor retrieval, ionospheric monitoring and the early warning of extreme weather, although GNSS signals are susceptible to various error sources, e.g. observation condition and space weather, making the data processing procedure be relatively complicated. The parameters reflecting the characteristics of ionospheric changes can be divided into the following two categories. The first are the parameters characterizing the large-scale variations of the ionosphere, which usually adopts the total electron content (TEC) over the station, which can be retrieved by geodetic receivers. The second are the ones representing small-scale ionospheric irregularities, e.g. S4, σ_ϕ. Scattering and diffraction phenomena are observed when GNSS signals pass through these ionospheric irregularities, leading to significant amplitude and phase fluctuation of the signals, which are called ionospheric scintillations. The ionospheric scintillation cannot be eliminated by the dual-frequency ionospheric-free combination, which is usually used as the basic observation in the GNSS positioning algorithm, making it be one of the main error sources affecting the position accuracy of GNSS during the current solar active period. The ionospheric scintillation index is a quantitative characterization of the ionospheric scintillation phenomenon. Accurate ionospheric scintillation factors can help monitor, model, and even eliminate the adverse effects of ionospheric scintillation on GNSS positioning.

Jiawang is a typical mined-out region in China and an important energy base in Jiangsu Province. With a coal mining history of over 130 years, Jiawang has produced a total of 360 million tons of coal and had 226 coal mines at its peak, resulting in 132,300 acres of subsided land. Currently, Jiawang has entered a new era of ecological restoration and transformation as its resources have been depleted. The key technological problems for high-quality ecological restoration and transformation of Jiawang include residual settlement control and prevention and the reconstruction of subsided wetland ecosystems. Monitoring settlement, atmospheric water vapor, and ionosphere is important for solving these key problems. Taking Jiawang as an example, our study area is located on the island in the middle of Pan'an Lake, Dawu Town, Jiawang District, Xuzhou, Jiangsu Province. The study area is 24 km away from Xuzhou City and the focus is on the quadrangle courtyard buildings on the island, with coordinates of 34°22'24"N and 117°23'09"E. The terrain in the area is flat, with the ground elevation generally between +30 to +31.5 meters and gradually decreasing from southwest to northeast. There is no river passing through the area, but due to the perennial waterlogging in the subsided area, Pan'an Lake Scenic Area was formed after renovation. We constructed a subsidence and spatial information monitoring system using GNSS and leveling technology to monitor surface settlement, atmospheric water vapor, and ionosphere activities in the subsidence area. The outcome is expected to provide technical support for regional high-quality ecological restoration and transformation.

2. Composition of the Monitoring System

The subsidence and spatial information monitoring system comprises a CHCNAV P5 geodetic GNSS receiver, a BDSSMART ionospheric scintillation monitoring receiver, and a set of hydraulic settlement meters. The on-site configuration and data outputs of the system are shown in Figure 1. The P5 and BDSSMART receivers are connected to the same CHCNAV C220GR choke-ring antenna in a zero-baseline configuration, but they are used for different purposes. The P5 geodetic receiver records multi-constellation GNSS observations at a sampling rate of 1 Hz. These observations are used for PPP-based coordinate estimation, atmospheric water vapor retrieval, and the calculation of TEC and related ionospheric indices. In contrast, the BDSSMART receiver is used specifically for ionospheric scintillation monitoring. It records GPS, GLONASS, BDS, and Galileo observations at a sampling rate of 50 Hz and provides the phase scintillation index σ_ϕ and amplitude scintillation index S4. Therefore, PPP processing in this study is performed using the observations collected by the P5 receiver rather than those from the BDSSMART receiver.

The observations collected by the two GNSS receivers are processed separately according to their respective functions. The 1 Hz observations recorded by the P5 geodetic GNSS receiver are used for PPP-based coordinate estimation and coordinate time-series analysis to determine the displacement of the GNSS station. The same P5 observations are also used to retrieve precipitable water vapor and calculate ionospheric parameters, including total electron content (TEC), the rate of TEC index (ROTI), the along-arc TEC rate index (AATR), and $\sigma_{\phi f,wavelet}$. In contrast, the 50 Hz observations recorded by the BDSSMART ionospheric scintillation monitoring receiver are processed using a sixth-order Butterworth filter to obtain the standard phase and amplitude scintillation indices, σ_{ϕ} and S_4, respectively. Thus, the PPP positioning and standard scintillation monitoring results are derived from different receiver data streams, although the two receivers share the same antenna.

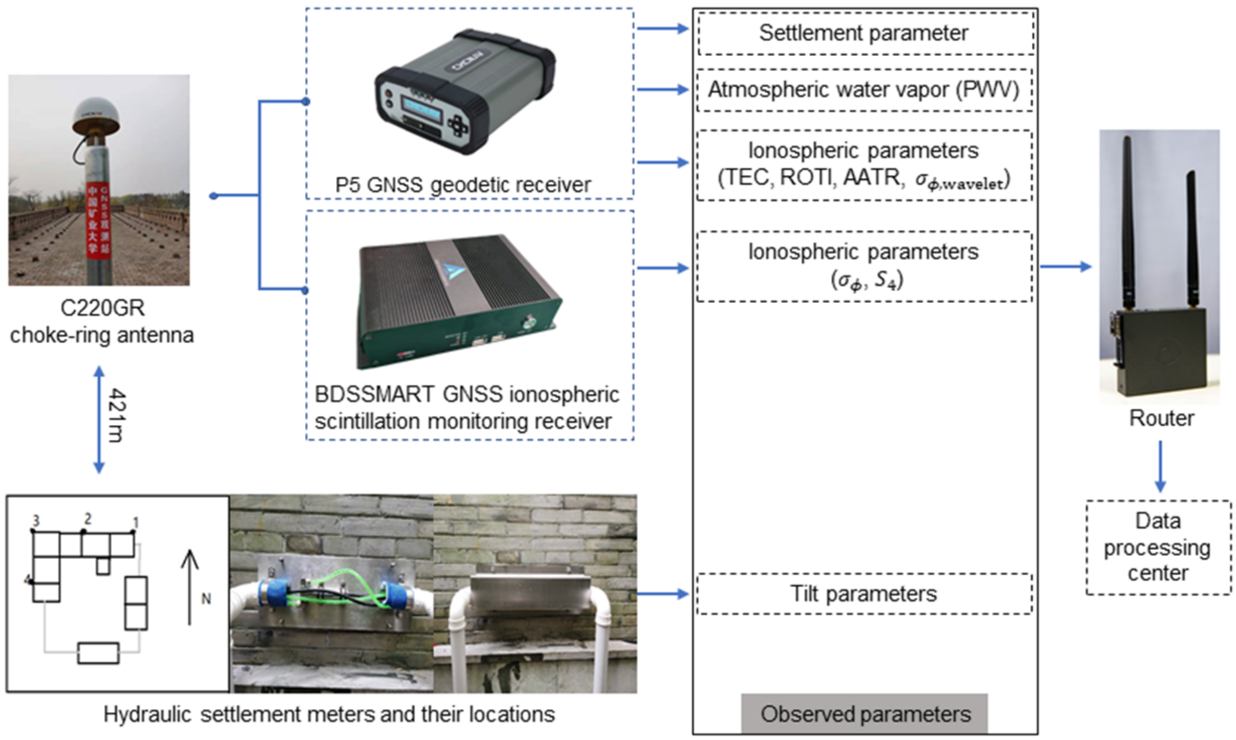

Fig. 1 Composition and output of the monitoring system

As only one GNSS station was installed at the site, only settlement parameters in the direction of the gravity line at the station can be obtained, and it is impossible to obtain the uneven subsidence rate of the buildings, i.e., the tilt parameters. To address this, we installed four CJ-1 hydraulic settlement meters on the side wall of a quadrangle courtyard building located about 421 meters away from the GNSS station on the lake island to automatically collect building settlement data. The relative positions of the GNSS station and the hydraulic settlement meters are shown in Figure 2, while a photograph of the installation is shown in the bottom left of Figure 1. The working principle of the CJ-1 hydraulic settlement meter is that when the height difference between the sensor and the fluid storage tank changes, the pressure on the sensing membrane changes accordingly, and the pressure causes deformation of the full-bridge silicon chip on the sensing membrane. The electric signal generated by the deformation is transmitted through the cable to the acquisition device, and the settlement change of the observation point can be measured. The sensor and the fluid storage tank are connected by a fluid pipe, and the pressure on the sensor is related to the height of the fluid level in the storage tank. The fluid storage tank comes with a silicon pressure sensor that measures the change in the fluid level in the tank to correct the measurement value of the observation point.

The GNSS geodetic receiver, ionospheric scintillation monitoring receiver, and hydraulic settlement meters mentioned above are connected to a router to establish a remote virtual local area network for remote control and online data transmission. All data is processed and calculated at the Data Processing Center of the School of Environment and Surveying Engineering at China University of Mining and Technology.

Fig. 2 Relative positions of the GNSS station and the hydraulic settlement meters

3. Data processing method

3.1 Data processing method for obtaining subsidence parameters using GNSS

To obtain subsidence parameters using GNSS data, the following steps can be taken. Step 1 involves data preparation, which includes observation files and corresponding parameter files for processing, such as precise ephemeris files (SP3), precise clock deviation files (CLK), code bias files (DCB), phase center correction files (ANTEX), and atmospheric and oceanic tide models. These models use the FES2004 model and the model proposed by Ray & Ponte [11].

The second step is data preprocessing, which can be divided into several processes. The first is quality control, which utilizes the Translation, Editing and Quality Checking (TEQC) software. TEQC is a powerful and user-friendly GNSS data preprocessing software developed by the UNAVCO Facility, a joint university consortium for satellite navigation and crustal deformation observation research in the United States. It offers free and open-source software services for GPS monitoring station data management in geoscience research. The quality of the data can be assessed based on completeness rate, signal-to-noise ratio, pseudorange multipath, cycle slip ratio [12][13], and ionospheric delay. In case of our GNSS station in Jiawang, where observation condition is relatively good, quality control may be skipped. The second is to detect and correct cycle slips using the TurboEdit method [14], which adopts Hatch-Melbourne-Wübbena (HMW) and phase ionospheric residual (PIR) combinations to detect cycle-slips [15][16]. Besides the process to obtain the subsidence parameters, it should be noted that cycle slip detection in the estimation of ionospheric and tropospheric parameters. Lastly, the third is to conduct elevation angle control and removal of short arc segments. Arc segments with less than 10 epochs are considered short and are removed to prevent interference in the solution [17][18][19][20]. The elevation angle is set at 10 degrees.

The third step is data processing, which involves using a self-developed platform for precise point positioning to calculate the daily coordinates of the observation station. The table below displays the specific processing strategies used.

Tab.1 PPP processing strategies

Items	Processing strategies
Observation Equation	Ionosphere-free combination
Elevation mask	10°

Stochastic model	Elevation angle weighted
Solid Earth tide	The second-order simplified tide model
Satellite clock	IGS precise clock product
Satellite and receiver antenna correction	Igs14.atx
Phase wind-up	Wu et al. 1993[21]
Relativistic effects	Beard and Senior 2017[22]
Tropospheric zenith delay (ZTD)	Estimated with Extended Kalman Filter (EKF)
Receiver clock error	Estimated with EKF
Coordinates of station	Estimated with EKF

The fourth step is to obtain settlement parameters by analyzing the coordinate sequence provided by the previous step. However, external conditions and signal transmission interference may generate a small number of outliers, which can interfere with the extraction of settlement trend items. To address this issue, the robust isolation detection method with interquartile range (IQR) is utilized to eliminate these outliers. Moreover, missing data can occur due to station maintenance or data transmission faults. We address this by using linear interpolation to fill in the gaps. However, since the missing data period is typically short, it has little impact on sequence analysis.

Following the removal of outliers and interpolation of missing values as described previously, linear fitting analysis is conducted using the least squares method, with the following fitting equation,

$$P(x) = a + bx \qquad (1)$$

where, a represents the initial value of the linear fitting, and b represents the rate of change resulting from the linear fitting. The rate of change calculated for the deformation in the vertical direction corresponds to the annual settlement parameter for the monitored station area. In addition to exhibiting long-term settlement or elevation trends, GNSS stations often display periodic variations in their coordinates. We employ cubic fitting to capture this periodic change.

3.2 Methodology for deriving settlement parameters using hydraulic settlement meters

When a structure being measured experiences settlement, the settlement amount (L) can be linearly related to the output reading F as follows,

$$L = \Delta F - \Delta B = (F - F0) - (B - B0) \qquad (2)$$

where, L is the settlement amount at the monitoring point of the hydraulic settlement gauge, measured in millimeters (mm); △F is the change in the real-time measurement value of the hydraulic settlement gauge relative to the reference value, in mm; △B is the change in the real-time measurement value of the liquid level in the storage tank relative to the reference value, in mm; F is the real-time measurement value of the hydraulic settlement gauge, in mm; F0 is the reference value of the hydraulic settlement gauge, in mm; B is the real-time measurement value of the liquid level in the storage tank, in mm; B0 is the reference value of the liquid level in the storage tank, in mm.

To determine the position of the hydraulic settlement gauge on the structure, a hydraulic settlement gauge marked with elevation is used, with H representing the elevation. The relationship between the settlement change of the hydraulic settlement gauge and the elevation is given by,

$$H = H0 - L / 1000 \qquad (3)$$

where, H is the real-time elevation of the hydraulic settlement gauge, in meters (m); H0 is the installation elevation of the hydraulic settlement gauge, in m. Note that the CJ-1 hydraulic settlement gauge has a temperature measurement function and outputs a signal as a digital quantity, which directly displays the physical quantity.

3.3 Method for monitoring regional precipitable water vapor (PWV)

The inversion of PWV from GNSS observation data can be divided into two steps: calculating the GNSS zenith wet delay (ZWD) and inverting PWV from the zenith wet delay. The ZWD is commonly determined by deducting the zenith hydrostatic delay (ZHD) from the zenith total delay, shown as follows,

$$ZTD = ZWD + ZHD \qquad (4)$$

For accurate retrieval of precipitable water, precise values of both ZTD and ZHD are necessary. ZTD is obtained through parameter estimation in PPP process as shown in Table 1, while ZHD can be accurately computed using models, such as the Saastamoinen model shown in the following equation,

$$\begin{cases} ZHD = 0.002277 \times \dfrac{P_s}{f(\varphi, h_s)} \\ f(\varphi, h_s) = 1 - 0.00266\cos(2\varphi) - 0.00028 h_s \end{cases} \quad (5)$$

where, φ denotes the latitude of the station; h_s represents its elevation; P_s indicates the surface pressure in mbar; e_s represents the surface water vapor pressure in mbar; and T_s denotes the absolute temperature at the surface.

Subtracting the ZHD given by Equation 5 from the ZTD yields the ZWD with high precision, while the PWV can be calculated from ZWD through the conversion parameter Π. Generally, ZWD can be denoted as follows,

$$ZWD = 10^{-6} \times (k_2^{'} + \frac{k_3}{T_m}) \times R_W \times IWV \quad (6)$$

where; $k_3 = (3.776 \pm 0.014) \times 10^5 K^2 \cdot hPa^{-1}$, $k_2^{'} = 16.48 K \cdot hPa^{-1}$, T_s denotes weighted average atmospheric temperature; R_W is the humidity gas constant, which is $461 J \cdot Kg^{-1} \cdot K^{-1}$; Integrated Water Vapor (IWV) represents the total amount of water vapor per unit area.

PWV refers to the amount of water vapor condensed into precipitation per unit area, and it is related to IWV as follows,

$$PWV = \frac{IWV}{\rho_{water}} = \Pi \cdot ZWD \quad (7)$$

where, the unit of PWV is mm; ρ_{water} denotes the liquid water density. Π is a dimensionless coefficient, which can be calculated as follows,

$$\Pi = \frac{10^6}{\rho_{water} R_W [(k_3 / T_m) + k_2^{'}]} \quad (8)$$

which shows that the precision of the inversed PWV is mainly determined by T_m. In Equations 4-8, P_s and T_m are the only two parameters which needs to be measured with local weather station or sounding data. However, those are not available at the GNSS station. Instead, we adopt an empirical model for troposphere delays, namely the Global Pressure and Temperature 3 (GPT3) model [23], to acquire P_s and T_m. The time and location are the input of GPT3, while it can provide mean values plus annual and semi-annual amplitudes of a set of quantities such as P_s, T_m and water vapor pressure. It should be noted that, because no collocated meteorological observations were available, the surface pressure used in the Saastamoinen model was derived from GPT3. Therefore, some regional modeling errors may remain in the estimated ZHD and PWV. Collocated pressure observations or a regionally calibrated ZHD model would be preferable when a quantitative assessment of absolute PWV accuracy is required.

3.4 Methods for monitoring regional ionospheric condition

The ionosphere is replete with numerous free electrons and ions due to the photoionization effect of sunlight. In normal circumstances, the ionization and recombination processes in the ionosphere achieve a state of equilibrium, leading to a stable electron density. However, disturbances can cause a significant and sudden increase or decrease in electron density in either global or local regions, resulting in the formation of plasma bubbles and irregularities. Given the intricate variations in electron density, this article employs multiple parameters to observe the ionosphere at various scales to investigate its changes.

3.4.1 Slant total electron content (STEC)

The slant total electron content (STEC) is estimated for each observational epoch along the line-of-sight between GNSS satellite and receiver using the carrier-phase smoothed pseudo-range method. This method is based on the geometry-free combination of pseudo-range and carrier phase observations with dual frequency, which is usually denoted as P_4 and Φ_4 respectively. We can adopt Φ_4 to smooth P_4 as follows,

$$P_4 = P_1 - P_2$$

$$\Phi_4 = \lambda_1 L_1 - \lambda_2 L_2 \quad (9)$$

$$\tilde{P}_4 = (P_4 + \Phi_4)_{arc} - \Phi_4 = I_1 - I_2 + DCB_r + DCB^s + \varepsilon$$

where, Pi denotes the pseudorange observation at frequency fi, L denotes the carrier-phase observation in cycles, λ is the corresponding wavelength, and $\Phi = \lambda i * Li$ represents the carrier-phase observation expressed in meters. $\tilde{P}_4$ denotes the pseudo-range smoothed with carrier phase observations; I_1 and I_2 represent ionospheric delay at frequency 1 and 2 respectively; DCB_r and DCB^s stand for differential code biases (DCB) of receiver and satellite respectively; The term ε represents the residual measurement error in the carrier-phase-smoothed geometry-free pseudorange combination, mainly including residual pseudorange noise and multipath effects, together with a comparatively small contribution from carrier-phase noise. Carrier-phase smoothing over a continuous cycle-slip-free arc can substantially reduce the random pseudorange noise but cannot eliminate it completely. Therefore, the residual noise term is retained in the observation model. $(P_4+\Phi_4)_{arc}$ is the average value of the sum of P_4 and Φ_4 in a continuous arc, to eliminate the effect of the ionosphere and calculate the float ambiguity together with DCB [24][25]. Equation 9 can be reformulated as an epoch iteration to make it suitable for real-time applications. Considering the relation between the ionospheric delay and STEC, the real STEC along the line-of-sight can be calculated as follows [25],

$$STEC = \frac{(f_1^2 f_2^2)}{40.3(f_1^2 - f_2^2)} \cdot (\tilde{P}_4 - DCB_r - DCB^s)$$

(10)

where, f_1 and f_2 denote the frequencies. The measurement noise is neglected in Equation 10. The DCB at the satellite is obtained from Center for Orbit Determination in Europe (CODE), while the DCB at the receiver is estimated by the method proposed by Jin et al [25].

3.4.2 Rate of TEC index (ROTI)

ROTI is the widely accepted scintillation index for monitoring ionospheric scintillation, based on low sampling frequency observation data. It has been utilized by numerous researchers and is defined as the standard deviation of the rate of STEC, shown as the following equations [26][27],

$$ROT = \frac{STEC(\mathrm{i}) - STEC(\mathrm{i}-1)}{T(\mathrm{i}) - T(\mathrm{i}-1)} \quad (11)$$

$$ROTI = \sqrt{\langle ROT^2 \rangle - \langle ROT \rangle^2} \quad (12)$$

where ROT stands for rate of TEC; T stands for time in the unit of minute; i means the ith epoch. The notation $\langle\cdot\rangle$ represents the expected value over a specific time interval, typically set to 1 or 5 minutes when calculating ROTI from observations with 1-s or 30-s sampling intervals respectively.

3.4.3 Along arc TEC rate index (AATR)

Instantaneous AATR is calculated by taking a weighted average of the ROTI values provided by all visible satellites at a given epoch, shown as follows [28][29],

$$AATR_k^j(t) = \frac{1}{(M(e))^2} \cdot \frac{\Delta STEC_k^j(t)}{\Delta t} \quad (13)$$

where $\Delta STEC$ stands for the variation of STEC between two consecutive epochs; j and k denotes the satellite and receiver respectively; Δt is the sampling interval; $M(e)$ represents the obliquity factor based on the satellite elevation angle e [30]. Then, the final AATR is calculated as the root mean square of all the instantaneous AATRs for all the visible satellites at the station during one-hour period, shown as follows,

$$RMS_{AATR,k}(T) = \sqrt{\frac{1}{N}\sum_{t=T}^{T+\Delta T}\sum_{k=1}^{n_{sat}(t)} (AATR_k^j(t))^2}$$

(14)

where N is total number of observations within the select period; ΔT is select as one hour; n_{sat} is number of visible satellites.

3.4.4 $\sigma_{\phi f,wavelet}$ index

Despite the introduction of the two indices mentioned above, i.e. ROTI and AATR, that facilitate the monitoring of ionospheric scintillation and regional ionospheric activity using geodetic receivers, the monitored results rely on dual-frequency combined observations and cannot estimate the effect of ionospheric disturbances on individual frequency. To solve this problem, the $\sigma_{\phi f,wavelet}$ index is proposed to extract the scintillation of each signals, through geodetic detrending and wavelet transform [31].

The first step to estimate the $\sigma_{\phi f,wavelet}$ index is to conduct geodetic detrending to carrier phase observations on each frequency. The aim of geodetic detrending is to obtain the residual containing only the ionospheric effect, which means the geometric distance and all the other error sources need to be eliminated from the original carrier phase measurements. The geometric distance is estimated with receiver coordinates given by the static precision point positioning and the satellite coordinated provided by international GNSS service (IGS) precise ephemeris product. The solid earth tide, satellite and receiver antenna error, satellite clock, phase wind-up, and relativistic effects are estimated with the models and products listed in Table 1, while the tropospheric effect and the receiver clock error are obtained with the output of PPP. After geodetic detrending, the residual of the carrier phase observation can be denoted as follows,

$$\hat{r}_f = I_f^r + I_f^d + B_f + \lambda_f N_f + \varepsilon_f \quad (15)$$

where $\hat{r}_f$ denotes the residual in the frequency f; I_f^r and I_f^d represent the ionospheric refraction and scintillation signal respectively; B_f is the hardware delay; λ_f is the wavelength of frequency f; and N is the ambiguity.

The next step involves denoising the data. It is important to minimize the effect of noise before extracting the scintillation signal, particularly when dealing with 30-second sampling interval observations. To achieve this, we utilize the Discrete Wavelet Transform (DWT) to decompose the residual, using the Daubechies wavelet with a vanishing moment of 2. A fixed-form threshold is then applied to the wavelet coefficients of the high-pass filters to eliminate the measurement noise. Finally, we apply the inverse discrete-time wavelet transform to the cleaned coefficients, resulting in a noise-reduced residual.

The third step involves separating the ionospheric scintillation signal from the denoised residual. Since the hardware delay and ambiguity are constant values in one observation arc, they can be easily separated in the frequency domain using the continuous wavelet transform (CWT) with Morse wavelet. After computing the CWT, the residual is transformed into a time-frequency matrix, where the coefficients corresponding to ionospheric scintillations are typically located in the middle frequency range, known as the characteristic frequency range of ionospheric scintillations, while the coefficients for ionospheric refraction are generally much lower. To extract the ionospheric scintillation signal, we use the coefficients located within the characteristic frequency range of ionospheric scintillation and apply the inverse continuous wavelet transform (ICWT). Finally, we can calculate the scintillation index based on the extracted scintillation signal as follows,

$$\sigma_{\phi f,wavelet} = \sqrt{\left\langle I_f^{d2} \right\rangle - \left\langle I_f^d \right\rangle^2} \quad (16)$$

where 60-s and 5-min are selected as the time range to calculate Equation 16 for 1-s and 30s sampling interval observations respectively.

3.4.5 σ_ϕ and S4 indices

The ionospheric scintillation monitoring receiver produces two standard outputs, i.e. the phase scintillation index (σ_ϕ) and the amplitude scintillation index (S_4). The amplitude scintillation index is determined by calculating the standard deviation of the detrended signal intensity normalized by its mean [32]. Meanwhile, the phase scintillation index is obtained by computing the standard deviation of the detrended carrier phase measurement. The equations for calculating S_4 and σ_ϕ are as follows,

$$S_4 = \sqrt{\frac{\langle SI^2 \rangle - \langle SI \rangle^2}{\langle SI \rangle^2}} \quad (17)$$

$$\sigma_\phi = \sqrt{\langle \phi^2 \rangle - \langle \phi \rangle^2} \quad (18)$$

where $\langle \cdot \rangle$ denotes the expectation within a specific time interval, typically set to 60 seconds. The signal intensity (SI) and carrier phase measurement (ϕ) are both detrended using a sixth-order Butterworth filter with a cutoff frequency of 0.1 Hz

4. Analysis of monitoring results

4.1 Analysis of Surface Deformation Monitoring Results

To analyze the results of surface deformation monitoring, we initially utilized GNSS data collected throughout 2022. However, the coordinates acquired using the PPP method in Section 3.1 are in the WGS84 coordinate system, representing geocentric Earth-Centered Earth-Fixed (ECEF) Cartesian coordinates, which do not directly indicate local surface deformation. Thus, converting these coordinates into local Cartesian coordinates, specifically the east-north-up coordinate system, is necessary. The transformation process requires using the latitude, longitude, and geodetic height of the GNSS station in the geodetic coordinate system as the origin on January 1, 2022, and utilizing a seven-parameter method to convert the ECEF coordinates in the WGS84 coordinate system to the north-east-up coordinate system [33]

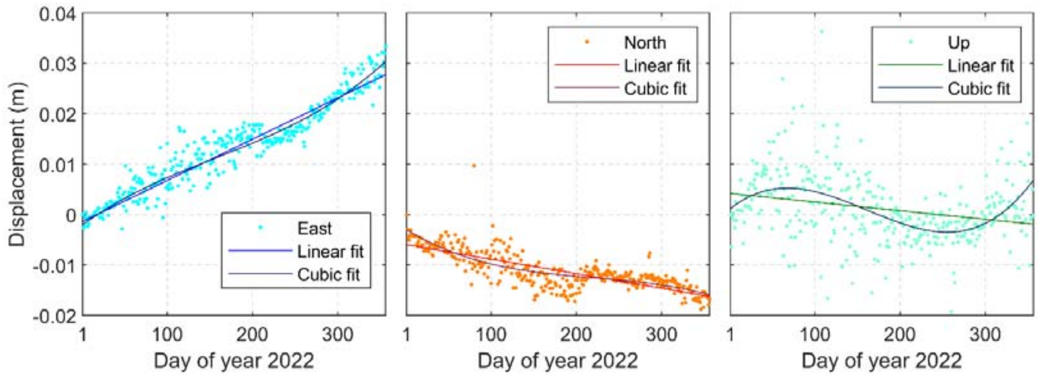

Fig. 3 Surface subsidence monitoring results and preliminary analysis based on 2022 GNSS data.

The coordinate changes of the GNSS station in the North-East-Up (NEU) coordinate system for the year 2022 are presented in Figure 3. To analyze the trends in the three directions, we conducted linear regression using the least squares method on the coordinate data. The results revealed that the station exhibited movement trends towards the East, South, and Down directions. Specifically, the rate of change in the East direction was 29.9 mm/year, the rate of change in the North direction was -10.5 mm/year, and the rate of change in the Up direction (height) was -6.3 mm/year. The estimated linear rates were 29.9 mm/year, −10.5 mm/year, and −6.3 mm/year in the east, north, and up components, respectively. These rates describe the motion of the GNSS station with respect to the reference frame adopted in the PPP solution. Because only one GNSS station was installed and no nearby stable reference station was included, the estimated rates may contain contributions from regional crustal motion, environmental loading, seasonal variations, and local deformation. Additionally, from the right panel of Figure 3, it was observed that the station exhibited a distinct periodic pattern of first rising and then lowering in the Up direction. The underlying cause of this characteristic may be complex, such as rebound caused by water pressure, which was beyond the scope of this study.

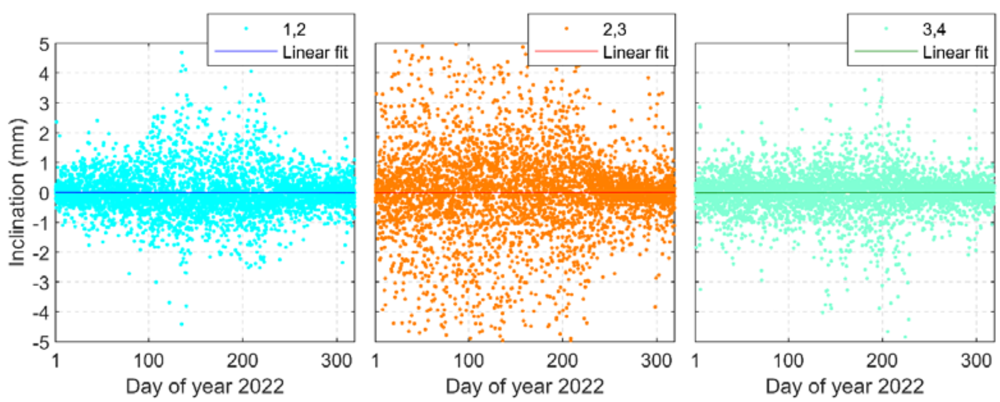

Fig. 4 Relative tilt variations based on measurements of the Hydraulic Settlement Meters in 2022.

In addition to ground subsidence, the tilt variations of buildings are also critical indicators for assessing the stability of mining subsidence areas. To monitor this, we utilized hydraulic settlement meters to measure the relative tilt changes between points 1 and 2, 2 and 3, and 3 and 4. The results for 2022 are shown in Figure 4. It can be observed that the instantaneous relative tilt variations between the points remained within ±5 mm, with higher measurement noise observed during the summer. We speculate that this might be due to the influence of temperature. To mitigate the interference of measurement noise and to better analyze the building's tilt variations over the year, we applied linear regression using the least squares method to the measurement results. The regression results for all points were zero, indicating that no tilt changes occurred in the building. This further suggests that the ground surface in the mining subsidence area remains stable.

4.2 Analysis of Regional Precipitable Water Monitoring Results

To evaluate the accuracy of atmospheric precipitable water monitoring in the region using the established GNSS monitoring station, we conducted a comparative analysis with a compact weather radar located on the rooftop of the Comprehensive Building at the Wenchang Campus of China University of Mining and Technology. This weather radar is positioned 45° northeast of the established GNSS station at a distance of 24 km. The weather radar is designed to detect the distribution center and leading edge of weather systems, primarily local severe weather such as cumulonimbus clouds and hail clouds, during the movement of clouds and precipitation. It provides precise data on the location, intensity, and other parameters of clouds and precipitation. By comparing the precipitation data measured by the weather radar with the water vapor information retrieved from the GNSS station, we can analyze the accuracy of the GNSS-based inversion results.

Figure 5 illustrates the temporal and spatial variation of rainfall monitored by the weather radar. To better visualize these changes, we created a 1-minute resolution rainfall animation (see attachment). Figure 6 depicts the time-series variation of precipitable water vapor (PWV) retrieved from the GNSS station. Combining Figure 5, the attached animation, and Figure 6, we analyze this precipitation event as follows:

The weather radar monitoring began at 21:00 on January 13, 2022, at which point no rainfall was observed at the monitoring site, though water vapor started to accumulate. An hour later, at 22:02, rainfall began, transitioning from light rain to moderate rain. This rainfall episode lasted for about an hour, until 23:02. During this period, a decrease in PWV was observed, but the arrival of a cloud mass rich in water vapor halted the reduction and initiated an increase in regional water vapor.

At 23:33, light rain resumed, transitioning to moderate rain by 23:42. However, the precipitation volume was smaller than the increase in water vapor, allowing the water vapor content to continue rising before subsequently decreasing. At 00:45 on January 14, moderate rain intensified into heavy rain, causing a rapid drop in water vapor content. This decline was particularly pronounced after 01:17, when heavy rain further intensified, accelerating the reduction of water vapor. The rainfall continued until 01:38, after which the water vapor content showed a continuous decreasing trend.

At around 02:10, the arrival of some clouds brought light rain, slowing the rate of water vapor reduction while maintaining the downward trend. Around 03:06, a small but water-vapor-rich cloud mass passed through the region, resulting in increased local rainfall and further slowing the decline in water vapor. This rainfall episode concluded at 03:45, during which the water vapor content decreased rapidly.

Subsequently, no significant water-vapor-rich clouds passed through the monitoring area, and the water vapor content continued to decrease. At 06:41, a cloud system originating from northwest Xuzhou passed over the monitoring station, halting the downward trend in water vapor. This cloud system brought light-to-moderate rainfall, which ended by 07:30, leading to a further decrease in water vapor.

From 08:30 onward, cloud cover was no longer prominent, but water vapor levels increased. Post-precipitation cooling and a decrease in cloud height rendered radar echoes ineffective. Following this accumulation, snowfall began in Xuzhou at approximately 10:00. Due to the radar's 7.2° elevation angle, the minimum detectable height in the monitoring area was around 3 km. At this point, cloud height fell below 3 km, preventing effective radar echoes.

The snowfall intensified as newly formed clouds passed through the monitoring site, slightly increasing water vapor, which peaked at 12:06. The snowfall persisted until 14:00, marking the end of this rain-to-snow event and initiating a prolonged phase of declining water vapor.

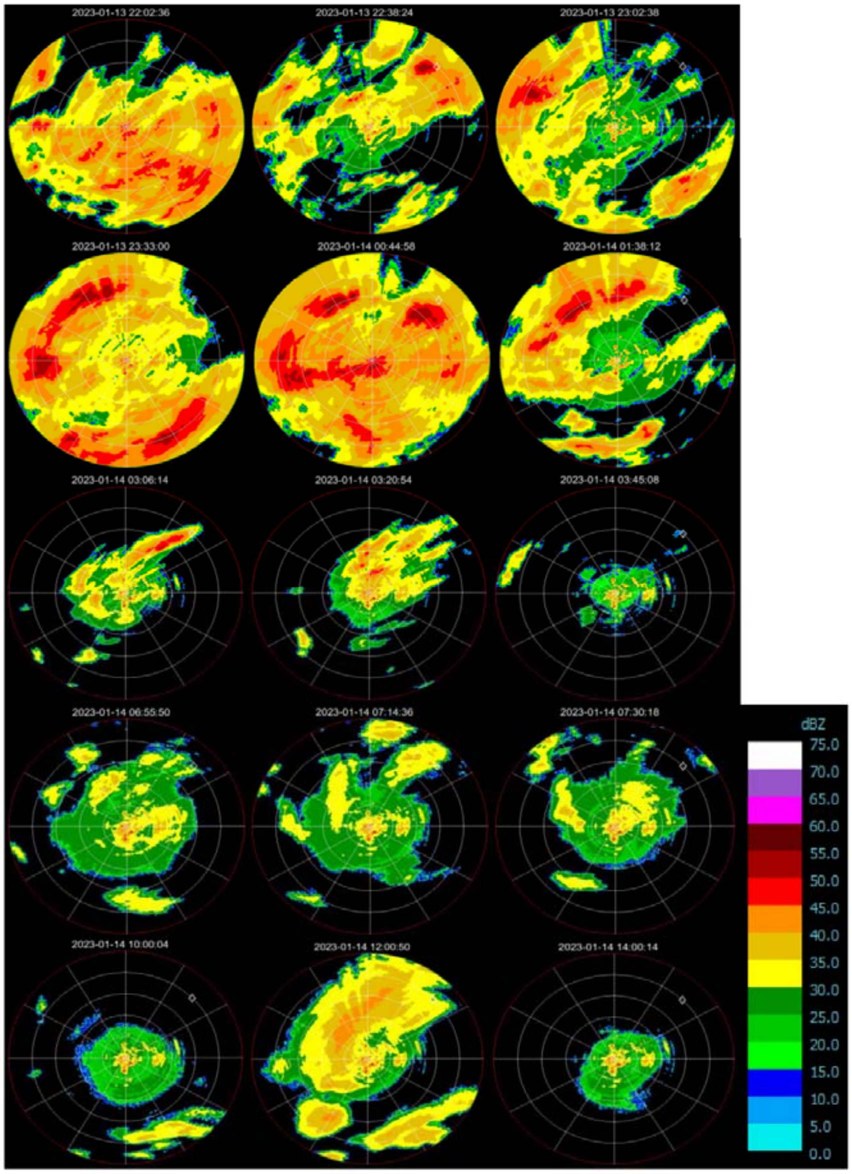

Fig. 5 Temporal and spatial variation map of rainfall monitored by weather radar.

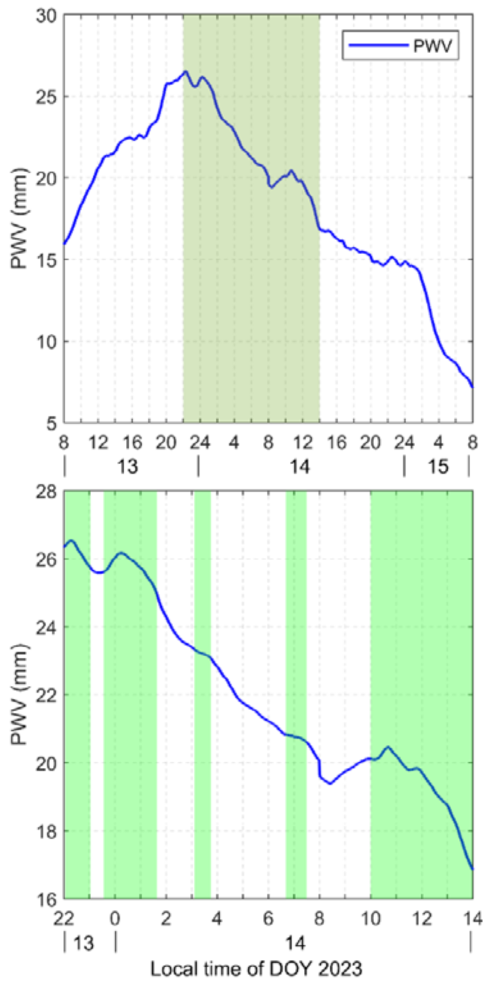

Fig. 6 PWV time-series variation based on GNSS.

This analysis demonstrates a strong coupling between atmospheric water vapor retrieved from the GNSS station and precipitation events. The high accuracy of the GNSS-derived water vapor data highlights its potential to support water vapor monitoring for ecological restoration in mining subsidence areas.

4.3 Analysis of the Ionospheric Response

To evaluate the effectiveness of the proposed $\sigma_{\phi f,wavelet}$ index in monitoring the ionospheric scintillation, this study analyzed GPS L1 carrier data from satellite PRN07 on Day 362 of 2022, between 14:00 and 19:00. By plotting the time-frequency spectrum of the $\sigma_{\phi f,wavelet}$ index, we assessed its responsiveness to ionospheric scintillation information and validated its accuracy by comparing it with the reference σ_{ϕ} index. As shown in the left panel of Figure 7, the time-frequency spectrum reveals that the largest magnitudes are concentrated below 0.02 Hz, reflecting the influence of ionospheric refraction effects during the observed arc segment. In the mid-frequency range (0.02 Hz–0.04 Hz), two peaks with large magnitudes appear at 14:42 and 18:49, corresponding to the characteristic frequency range of ionospheric scintillation [15]. The right panel demonstrates that at these same time points, the $\sigma_{\phi f,wavelet}$ index exhibits disturbance trends consistent with the reference σ_{ϕ} index, confirming the capability of $\sigma_{\phi f,wavelet}$ to effectively monitor ionospheric scintillation. Furthermore, during the observation period, the satellite elevation angle for this arc segment remained above 30°, ensuring that the two mid-frequency peaks were caused by ionospheric scintillation rather than multipath effects.

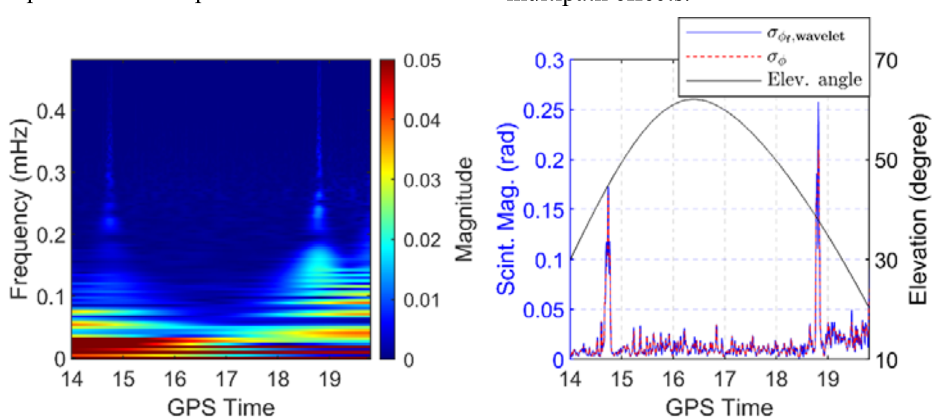

Fig. 7 Analysis of the accuracy of $\sigma_{\phi f,\text{wavelet}}$ index in monitoring scintillation.

Ionospheric scintillation is related to geomagnetic and solar activity [34][35]. Therefore, this study selected three-hour magnetic indices (Kp), solar 10.7 cm radio flux (F10.7), and the Dst index of geomagnetic storms to characterize space weather conditions. The Kp index is derived from the average geomagnetic horizontal component disturbance levels measured at 13 global geomagnetic observation stations. It serves as an important indicator of the energy input from solar wind to Earth, with Kp ≥ 5 typically indicating the occurrence of a geomagnetic storm. The F10.7 index represents the solar radio flux at a wavelength of 10.7 cm (2800 MHz), which is a key parameter for describing quiet solar radiation intensity. When F10.7 ≥ 150 sfu, it is considered a period of high solar activity. The Dst index is obtained by averaging the disturbance in the H-component of the geomagnetic field measured at four low-latitude magnetic observatories. A Dst ≤ -30 nT is considered to indicate the occurrence of a geomagnetic storm.

Data from Days 359 to 362 of 2022 were selected to study the response of the scintillation factor to space weather events, with the corresponding space weather conditions shown in Figure 8. Influenced by both coronal mass ejections and high-speed solar wind streams from coronal holes, the Dst index reached its minimum of -32 nT at 20:00 on Day 359, indicating a minor geomagnetic storm. On Day 360, the Kp index remained at minor storm levels for three consecutive hours between 13:00 and 15:00. Both Days 361 and 362 were characterized by high solar activity, leading to moderate geomagnetic activity.

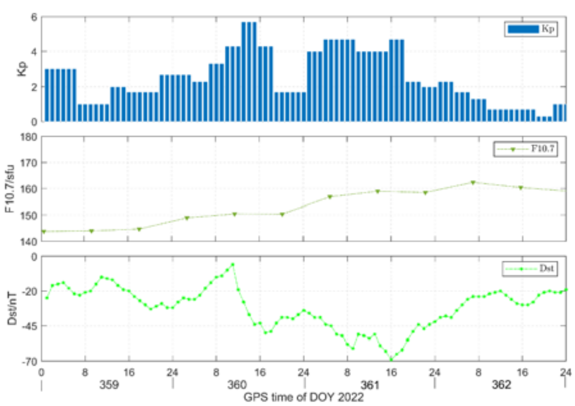

Fig. 8 Space Weather Conditions from Days 359 to 362 of 2022

Figure 9 shows the fluctuations of total electron content (TEC) and ionospheric disturbance indices for each satellite during Days 359 to 362. Given the close relationship between ionospheric scintillation and the day-night cycle [36], this study used an astronomical algorithm with atmospheric refraction effect correction [37] to determine the day-night variation in the region. The shaded areas in the figure represent nighttime, while the non-shaded areas indicate daytime. Additionally, the satellite elevation angles for both STEC and various ionospheric disturbance indices remained above 30° to ensure that the detected disturbances were primarily due to ionospheric scintillation rather than multipath effects.

The mean STEC in Figure 9 represents the average STEC value after suppressing the interference caused by the satellite elevation angle using the mapping function in Equation 13 [30]. It clearly shows a day-night variation pattern. This is because solar radiation during the day increases ionization, which raises the number of free electrons in the atmosphere, leading to higher electron density and the formation of the day-high, night-low phenomenon depicted in the figure. The AATR measures the average state of ionospheric disturbance over a large spatial area [38], and is closely related to changes in electron density. Therefore, it exhibits a similar variation trend to the STEC. The ROTI index remained stable throughout the observation period, with no significant fluctuations even during the geomagnetic storm, indicating that the ROTI index is less suitable for monitoring ionospheric scintillation in mid-latitude regions.

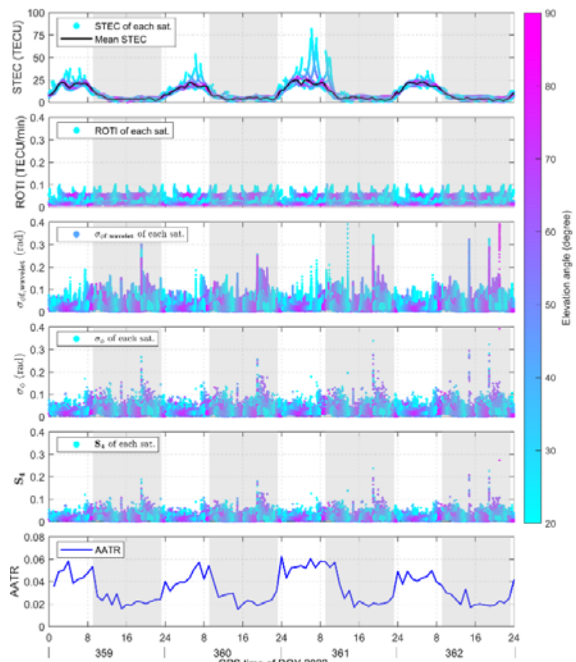

Fig. 9 Fluctuations of Total Electron Content and ionospheric disturbance indices from Days 359 to 362 of 2022.

The $\sigma_{\phi f,wavelet}$ index, along with the reference σ_{ϕ} and S_4 indices, showed good consistency. A slight ionospheric scintillation phenomenon was observed approximately 9 hours after sunset, which coincided with the timing of the geomagnetic storm observed in Figure 8. This phenomenon may be attributed to the irregular structures in the ionosphere over the equator diffusing along magnetic field lines to mid-latitude regions. As these irregular structures gradually weaken or even dissipate, ionospheric scintillation in the mid-latitudes tends to occur predominantly at night, with relatively low scintillation intensity [39].

5 Conclusion

This study developed a subsidence and spatial information monitoring system for mined-out regions. The system utilizes the relative position tilt from hydraulic settlement meters and settlement parameters obtained from GNSS data for subsidence monitoring, while also employing GNSS station-derived atmospheric precipitable water vapor (PWV) for atmospheric moisture monitoring and various ionospheric scintillation factors computed by GNSS receivers for ionospheric scintillation monitoring. By integrating subsidence, atmospheric water vapor, and ionospheric disturbance monitoring, the system provides complementary observational information for the Jiawang mined-out area. The subsidence and relative-tilt measurements support the assessment of residual ground deformation and structural stability; the GNSS-derived PWV reflects regional atmospheric moisture variations and precipitation processes; and the ionospheric parameters help assess the effects of space-weather disturbances on the reliability of GNSS-based positioning and deformation monitoring. Therefore, the system provides technical and observational support for ecological restoration management and the safe utilization of the restored mined-out area, rather than a direct theoretical foundation for ecological restoration.

The PPP-derived coordinate time series showed linear rates of 29.9 mm/year, −10.5 mm/year, and −6.3 mm/year in the east, north, and up components, respectively. These values represent the absolute motion of the GNSS station in the adopted reference frame and cannot be attributed solely to local mining-induced subsidence because no nearby stable regional reference station was included. In contrast, the hydraulic settlement measurements showed no significant long-term relative tilt among the monitored points of the building during the observation period.

The atmospheric moisture inversion results are consistent with the meteorological radar monitoring data and accurately reflect the changes in regional moisture. Compared to meteorological radar, the atmospheric moisture inversion has a higher resolution, reaching 30 seconds, while the radar's resolution is limited to a maximum of 5 minutes. It is worth noting that the rainfall dynamic map has a resolution of approximately 1 minute. However, when cloud height decreases, the coverage of the meteorological radar is reduced. Additionally, the GNSS monitoring results are more precise and cost-effective, with the cost being only one-tenth that of meteorological radar.

To validate the accuracy of the ionospheric scintillation monitoring using the $\sigma_{\phi f,wavelet}$ index extracted from 30-second GNSS data, this study compared it with the reference σ_{ϕ} and S_4 indices. The results demonstrate that the $\sigma_{\phi f,wavelet}$ shows a consistent disturbance trend with the reference values, successfully detecting ionospheric scintillation driven by geomagnetic disturbances, solar activity, and other factors. Furthermore, the ionospheric parameters effectively represent the day-night variation patterns of ionospheric scintillation over short time periods.

Acknowledgments

This research was supported by National Natural Science Foundation of China (Nos. 42674032, 42274021, 42361134583), the China Postdoctoral Science Foundation (No. 2023M743762, 2024T171001), the Independent Innovation Project of "Double-First Class" Construction (No. 2022ZZCX06), and 2022 Jiangsu Provincial Science and Technology Initiative-Special Fund for International Science and Technology Cooperation (No. BZ2022018).

6 References

[1] JU Wei, JIANG Bo, QIN Yong, et al., The present-day in-situ stress field within coalbed methane reservoirs, Yuwang Block, Laochang

Basin, south China, Marine and Petroleum Geology. 102 (2019) 61–73.

[2] ZHANG Peng, MENG Ya, LIU Chaoying, et al., In-situ stress of coal reservoirs in the Zhengzhuang area of the southern Qinshui Basin and its effects on coalbed methane development, Energy Geoscience. 4(7) (2023a) 100144.

[3] ZHANG Hongxing, YUAN Yunbin, LI Wei, et al., A Real-Time Precipitable Water Vapor Monitoring System Using the National GNSS Network of China: Method and Preliminary Results, IEEE Journal of Selected Topics in Applied Earth Observations and Remote Sensing. 12(5) (2019) 1587-1598.

[4] GHAUSI S A, ZEHE E, GHOSH S, et al., Thermodynamically inconsistent extreme precipitation sensitivities across continents driven by cloud-radiative effects, Nature Communications. 15 (2024) 10669.

[5] LI Chuxuan, HANDWERGER A L, HORTON D E, Mixed Hydrometeorological processes explain regional landslide potential, Geophysical Research Letters. 52 (2025) e2025GL115912.

[6] DUAN Yu, DING Mingtao, HE Yufeng, et al., Projections of global road risk exposed to landslides under climate change, Communications Earth & Environment. 7 (2026) 57.

[7] XIONG Jing, HAN Fei, Positioning performance analysis on combined GPS/BDS precise point positioning, Geodesy and Geodynamics. 11(1) (2020) 78-83.

[8] ZHAO Dongsheng, LI Wang, LI Chendong, et al., Extracting an ionospheric phase scintillation index based on 1 Hz GNSS observations and its verification in the Arctic region, Acta Geodaetica et Cartographica Sinica. 50(3) (2021) 368-383.

[9] LI Wang, JIANG Yiping, JI Hongyuan, et al., Amplitude scintillation detection with geodetic GNSS receivers leveraging machine learning decision tree, Satellite Navigation. 5 (2024) 18.

[10] HUANG Jiande, LI Xingxing, LI Xin, et al., Quality monitoring of grid-based atmospheric corrections in GNSS PPP-RTK service using leave-one-out cross-validation, Satellite Navigation. 6 (2025) 25.

[11] RAY R D, PONTE R M, Barometric tides from ECMWF operational analyses, Annales Geophysicae. 21 (2003) 1897–1910.

[12] CHANG Guobin, XU Tianhe, YAO Yifei, et al., Ionospheric delay prediction based on online polynomial modeling for real-time cycle slip repair of undifferenced triple-frequency GNSS signals, Measurement. 146 (2019) 289–297.

[13] ZHANG Zhetao, YUAN Haijun, HE Xiufeng, et al., Cycle slip detection and repair based on the unmodeled-error-constrained geometry-free combining geometry-based models for a single-frequency receiver, Measurement. 217 (2023b) 113090.

[14] BLEWITT G, An automatic editing algorithm for GPS data, Geophysical Research Letters.17(3) (1990) 199-202

[15] ZHAO Dongsheng, ZHANG Xueli, LI Wang, et al., Extracting ionospheric phase scintillation indicator from GNSS observations with 30-s sampling interval in the high-latitude region, GPS Solutions. 27 (2023) 79.

[16] SUN Shuang, CHAI Hongzhou, WANG Min, et al., Real-time multi-GNSS and mixed-frequency cycle slip detection and repair method based on geometry-based and geometry-free models with improved algorithm, Advances in Space Research. 77(7) (2026) 7650–7668.

[17] ZHAO Dongsheng, LI Wang, LI Chendong, et al., Ionospheric phase scintillation index estimation based on 1 Hz geodetic GNSS receiver measurements by using continuous wavelet transform, Space Weather. 20(4) (2022a) e2021SW003015.

[18] HE Shengping, HOBIGER Thomas, BECKER Doris, Improving PPP positioning and troposphere estimates using an

azimuth-dependent weighting scheme, GPS Solutions. 28 (2024) 212

[19] HAMZA V, STOPAR B, STERLE O, et al., Observations and positioning quality of low-cost GNSS receivers: a review, GPS Solutions. 28 (2024) 149.

[20] GUO Zihuai, YAO Yibin, FENG Qian, et al., GNSS robust algorithm based on elevation-error statistical feature for deformation monitoring, Measurement. 259(B) (2026) 119671.

[21] WU JT, WU SC, HAJJ GA, BERTIGER WI, LICHTEN SM, Effects of antenna orientation on GPS carrier phase. Manuscripta Geodaetica 18(2) (1993) 91–98

[22] BEARD R, SENIOR K (2017) Clocks. In: Teunissen PJG, Montenbruck O (eds) Springer Handbook of global navigation satellite systems. Springer, Cham, pp 121–164

[23] LANDSKRON D, BÖHM J, VMF3/GPT3: refined discrete and empirical troposphere mapping functions, Journal of Geodesy. 92(3) (2018) 349–360.

[24] LI Wang, YUE Jianping, GUO Jinyun, et al., Statistical seismo-ionospheric precursors of M7.0+ earthquakes in Circum-Pacific seismic belt by GPS TEC measurements, Advances in Space Research. 61(5) (2018) 1206–1219..

[25] JIN Rui, JIN Shuanggen, FENG Guiping, M_DCB: Matlab code for estimating GNSS satellite and receiver differential code biases, GPS Solutions. 16 (2012) 541-548.

[26] PI X, MANNUCCI A J, LINDQWISTER U J, et al., Monitoring of global ionospheric irregularities using the Worldwide GPS Network, Geophysical Research Letters. 24(18) (1997) 2283-2286.

[27] ZHAO Dongsheng, WANG Qianxin, LI Wang, et al., Validating Ionospheric Scintillation Indices Extracted from 30s-Sampling-Interval GNSS Geodetic Receivers with Long-Term Ground and In-Situ Observations in High-Latitude Regions, Remote Sensing. 14(17) (2022b) 4255.

[28] JUAN J M, SANZ J, ROVIRA-GARCIA A, et al., AATR an ionospheric activity indicator specifically based on GNSS measurements, Journal of Space Weather and Space Climate. 8 (2018) A14.

[29] WILKEN V, KRIEGEL M, JAKOWSKI N, et al., An ionospheric index suitable for estimating the degree of ionospheric perturbations, Journal of Space Weather and Space Climate. 8 (2018) A19.

[30] NGUYEN V K, ROVIRA-GARCIA A, JUAN J M, et al., Measuring phase scintillation at different frequencies with conventional GNSS receivers operating at 1 Hz, Journal of Geodesy. 93(10) (2019) 1985–2001.

[31] ZHAO Dongsheng, LI Wang, LI Chendong, et al., Analysis on the ionospheric scintillation monitoring performance of ROTI extracted from GNSS observations in high-latitude regions, Advances in Space Research. 69(1) (2022c) 142-158.

[32] VAN DIERENDONCK A J, KLOBUCHAR J, HUA Q, Ionospheric scintillation monitoring using commercial single frequency C/A code receivers [C]// Proceedings of the 6th International Technical Meeting of Satellite Division of the Institute of Navigation (ION GPS 1993), Salt Lake City, UT. (1993) 1333-1342.

[33] SUN Xiaorong, ZHANG Shubi, XU Aigong, et al., Applicability analysis of seven-parameter coordinate transformation model, Science of Surveying and Mapping.37(6) (2012) 38-39.

[34] JIN Yaqi, MOEN J I, MILOCH W J, et al., Statistical study of the GNSS phase scintillation associated with two types of auroral blobs, Journal of Geophysical Research:Space Physics. 121(5) (2016) 4679-4697.

[35] ZHAO Dongsheng, ZHANG Peicheng, ZHANG Xueli, et al., MISSION: a MATLAB-based software for multi-GNSS ionospheric scintillation index calculation and andanalysis. GPS Solutions, 30 (2026) 8.

[36] LIU Kun, SHENG Dongsheng, SUN Shuji, et al., Statistical characteristics of ionospheric scintillation in China based on the data of GNSS during 24th solar cycle (in Chinese), Chinese Journal of Space Science. 41(4) (2021) 562-567.

[37] MEEUS J, Astronomical Algorithms, 2nd Edition. Willmann-Bell Inc, Richmond, Virginia, USA December 1999.

[38] BERNGARDT O I, VOEYKOV S V, PEREVALOVA N P, Comparison of the TEC-based ionospheric disturbance indices AATR and WTEC, Journal of Atmospheric and Solar-Terrestrial Physics. 203(C) (2020) 105254.

[39] WANG Ning, GUO Lixin, ZHAO Zhenwei, et al., A comparative study of ionospheric spread-F and scintillation at low- and mid-latitudes in China during the 24th solar cycle, Advances in Space Research. 63(2) (2019) 986-998.

Authors

Dongsheng Zhao is a Specially Appointed Research Professor at the School of Environment and Spatial Informatics, China University of Mining and Technology. He received his Ph.D. degree from the University of Nottingham and his B.Eng. degree from Wuhan University. His research focuses on GNSS remote sensing, particularly ionospheric scintillation monitoring and modeling.

Hao Liu is currently pursuing his PhD degree at China University of Mining and Technology. His research interests include ionospheric scintillation monitoring, forecasting, and GNSS positioning integrity.

Qianxin Wang is a Professor at the School of Environment and Spatial Informatics, China University of Mining and Technology. His research interests include GNSS precise positioning, multi-system GNSS data processing, high-precision satellite orbit determination and geodetic data analysis.

Kefei Zhang is a Professor at the School of Environment and Spatial Informatics, China University of Mining and Technology. He received his Ph.D. degree from Curtin University, Australia. His research interests include GNSS atmospheric modeling, space mining and precision agriculture.

Jianfeng Zha is a Professor at the School of Environment and Spatial Informatics, China University of Mining and Technology. He received his Ph.D. degree from China University of Mining and Technology. His research interests include machine-vision-based deformation monitoring, UAV-LiDAR surface subsidence monitoring, mining subsidence prediction and disaster prevention.

Craig M. Hancock is a Professor in Geospatial Engineering at the School of Architecture, Building and Civil Engineering, Loughborough University. His research interests include GNSS error mitigation, ionospheric monitoring, structural health monitoring and digital construction.